Mechanical Systems and Signal Processing 211 (2024) 111245

Contents lists available at ScienceDirect

Mechanical Systems and Signal Processing

journal homepage: www.elsevier.com/locate/ymssp

Real-time monitoring of the interelectrode gap during electrochemical machining processes using a smart machine tool equipped with an optical fiber Fabry-Pérot interferometer: Principle and application

Fengfeng Zhou, Siying Chen, Xingyu Fu, Martin B.G. Jun *

School of Mechanical Engineering, Purdue University, 585 Purdue Mall, West Lafayette 47907-2088, USA

ARTICLE INFO

Keywords:
Electrochemical machining
Spectrum analysis
Optical interferometer
Optical fiber sensor

ABSTRACT

Being a problem that has long plagued the field of electrochemical machining process, real-time and high precision monitoring of the interelectrode gap is a difficult task. In this research, we introduce a method for monitoring the interelectrode gap using a tool electrode equipped with an optical fiber sensor. This method does not require large numbers of parameters such as conductivity of the electrolyte, electric current density distribution, shape of the electrodes, etc. and therefore reduces the complexity of the monitoring system. The optical fiber, moving together with the tool, forms an open Fabry-Pérot interferometer consists of a reflection surface of the fiber end and a reflection surface of the workpiece. Additionally, we introduce a spectrum analysis method specifically designed for the Fabry-Pérot interferometer spectrum. This method provides the absolute distance between the optical fiber and the target, demonstrating robustness to noise and abrupt spectrum changes. Consequently, it can be utilized in harsh environments for high-precision distance monitoring, a task challenging for traditional methods using optical interferometers. With the proposed method, a difference of ±2.5 μm was achieved compared with demodulating the spectrum manually. The average process time of a spectrum with 16,001 sampling points and a distance resolution of 1 nm is 0.148 s. Real-time monitoring and control of an electrochemical machining process was also implemented. The interelectrode gap was successfully maintained at 200 ± 5 μm throughout the machining process and the final machining depth measured by the proposed method and an optical measurement system has a difference of 6 μm.

1. Introduction

The Electrochemical Machining (ECM) process is a non-traditional method that removes material through electrochemical reactions. Compared with traditional methods, it has advantages in machining difficult-to-machine materials, such as titanium, tungsten, and nickel-based alloys. Moreover, the machining process does not introduce residual stress, heat-affected zones, extra deformation, or surface damage [1–6]. The machining process can also be controlled with a high flexibility by adjusting the machining voltage/current, interelectrode gap (IEG), and the electrolyte [7]. Therefore, ECM is a promising method for high-quality manufacturing of

* Corresponding author.
E-mail address: mbgjun@purdue.edu (M.B.G. Jun).

https://doi.org/10.1016/j.ymssp.2024.111245
Received 18 September 2023; Received in revised form 5 February 2024; Accepted 8 February 2024
Available online 15 February 2024

metals and other conductive materials. The IEG serves as an essential parameter influencing the machining process, product quality, and even system safety. So, the monitoring of the IEG has become an urgent task, as the current estimation of the IEG relies on multiple parameters such as the type and conductivity of the electrolyte, the pH, the shape of the machining tool, temperature, electric current density distribution, and more. Monitoring these parameters lead to a complex monitoring system, making it both unaffordable and less robust. Furthermore, even with an advanced monitoring system, the typical tolerance zone still remains within ± 25 μm. While ultrasonic monitoring directly provides the IEG, it is limited to IEG values greater than 400 μm, exceeding the typical range for most ECM processes [8]. Therefore, to improve its application in high-performance manufacturing scenarios, a method to directly monitor the IEG in real-time and with high precision is needed. Optical interferometers measure the distance using the interference of light, which can easily reach a resolution of nanometer scale. Comparing Fabry-Pérot interferometers (FPIs), Michelson interferometers (MIs), and Mach-Zehnder interferometers (MZIs), which are widely used for high precision monitoring, FPIs have a simple structure, usually exhibit a better signal-to-noise ratio due to their multibeam interference nature, and can be used as a probe when utilizing their reflection spectrum. Therefore, FPI will be used to monitor the IEG in this research.

Nowadays, high precision monitoring technology has become the cornerstone of modern research and production. With the increasing demand for high precision monitoring from macro-scale gravitational wave detection (such as LIGO [9], VIRGO [10], and KAGRA [11]) to micro-scale tasks like holographic lithography [12–14] and biomedical monitoring [15–17], optical interferometers become a promising tool due to its qualities of high sensitivity, high accuracy, immunity to electromagnetic wave interference, just to name a few. Due to its sensitivity to environmental changes, interference spectra are often utilized for environmental monitoring [18–20]. These spectra are usually obtained from a spectrometer, which uniformly samples the light intensity in the wavelength domain. Various spectrum analysis methods have been developed to extract the optical distance information of the interferometers. One time-honored approach is tracking the shift of the peaks or troughs of the interference spectrum [21–23]. However, this method only provides information about change in optical distance. Additionally, tracking peaks or troughs becomes challenging when the spectrum is noisy, or the optical distance undergoes a significant change. Another method, Fourier Transform (FT), is used by many researchers to analyze the spectrum since the interference pattern exhibits a periodic appearance [24,25]. But this method is limited to a narrow wavelength range because the spectrum is not a strict periodic function with respect to wavelength. This is because the Free Spectrum Range (FSR) of the spectrum varies with wavelength since the wavelength term is in the denominator of the trigonometric function [26]. Efforts have been made to develop interferometers with strict periodic interference spectra across the wavelength domain [27,28], but these methods are not readily accessible to most research groups and manufacturers.

To overcome these challenges, we developed a method that effectively handles extremely noisy spectra and accurately determines the optical distance between the two reflection mirrors (optical cavity length) in FPIs. As the mathematical foundation, we developed a spectrum decomposition method with a basis of chirped functions. We call it the Reciprocal Fourier Transform (RFT) method in the paper. We also developed the discrete form of RFT (DRFT) for computer analysis. To improve efficiency, a transform was developed to map the spectrum from the original space to its reciprocal space, allowing the use of the highly efficient Fast Fourier Transform (FFT). We call this method the Reciprocal Fast Fourier Transform (RFFT) method. To further improve the resolution of the optical cavity length, the uncertain range given by the RFFT was divided into small segments and the cross-correlation between the experimental spectrum and the theoretical spectra with different optical cavity lengths were calculated. The optical cavity length of the theoretical spectrum that has the maximum cross-correlation is used as the measurement of the experimental spectrum. Finally, the proposed method was applied to determine the IEG of an electrochemical machining (ECM) process. The result shows that this method can give the optical cavity length with high efficiency, high accuracy, and high resolution. The proposed method offers a systematic solution enabling the use of optical interferometers in noisy and rapidly changing spectra. In contrast, traditional methods may lose track of the peaks or troughs of the spectrum under the same conditions, limiting their applications. This algorithm is particularly useful for analyzing a wide range of interference spectra, especially in environments with significant disturbances, such as those encountered in vehicles, aircraft, and chemical reactions.

2. Method

To overcome the limitations of the time-honored peak tracking algorithm, we developed a decomposition method using a group of chirped functions as basis to reveal the mathematical structure of the spectrum. In order to improve the analyzing efficiency, we developed a new transform that maps the spectrum into a format that is compatible with the highly effective FFT algorithm. At last, we will introduce a method to enhance the resolution in the analysis of the spectrum.

2.1. The continuous reciprocal Fourier transform

Before introducing the analysis method, we first construct the Fourier series for an oscillating signal with a variable period. Pryjmak [29] investigated the oscillating signals with a variable period and the orthogonality of the trigonometric functions with a form of $\cos(x^\alpha)$ and $\sin(x^\alpha)$ where $x \geq 0, x \neq 1$, and $\alpha > 0$ was proved. This orthogonality also applies when $\alpha = -1$ following the same process.

For a strictly periodic signal, the period is a constant and the direction of the period is not defined. Here, we encounter a function of $f(x) = \cos(m/x)$ where m are nonnegative integers. For this function, it has a variable period of which the direction will appear naturally during the following duction.

Consider a set of functions $p_m(x) = \cos(m/x)$ and $q_m = \sin(m/x)$, $x > 0$. Let $p_m(x + h(x)) = p_m(x)$, we have [29]:

$$h_m(x) = -x + \frac{mx}{m + 2\pi x} < 0, \tag{1}$$

where the continuous function $h(x)$ is the variable period of function $p_m(x)$. $h_m < 0$ indicates the variable period is toward the negative direction along the x axis. Take inner product of p_m and q_m with respect to weight function $w(x) = 1/x^2$, we have:

$$< p_m, p_n >_w = \int_{x_0+h_1(x_0)}^{x_0} \frac{1}{x^2}\cos\left(\frac{m}{x}\right)\cos\left(\frac{n}{x}\right)dx = \begin{cases} 0, & \text{if } m \neq n \\ \pi, & \text{if } m = n > 0 \end{cases}. \tag{2}$$

Likewise, we have:

$$< p_m, q_n >_w = 0, \quad \text{and} \quad < q_m, q_n >_w = \begin{cases} 0, & \text{if } m \neq n \\ \pi, & \text{if } m = n > 0 \end{cases} \tag{3}$$

When $m = n = 0$, we have $< p_m, p_m >= 2\pi$ and $< q_m, q_m >= 0$. Therefore, elements in set $\{p_m(x), q_m(x)\}$ are orthogonal with respect to $w(x) = 1/x^2$. Expand $f(x)$ with basis p_m and q_m, the Fourier coefficients are:

$$\begin{aligned} a_m &= \frac{< f(x), p_m(x) >_w}{\| p_{m(x)} \|_w^2}, \\ b_m &= \frac{< f(x), q_m(x) >_w}{\| q_{m(x)} \|_w^2}. \end{aligned} \tag{4}$$

We have $f(x) = \sum_{n=0}^{\infty}[a_n p_n(x) + b_n q_n(x)]$. Replacing $\sin(m/x)$ and $\cos(m/x)$ with $\exp(\pm im/x)$ according to Euler equation, we have the complex form:

$$f(x) = \sum_{m=-\infty}^{\infty} c_m e^{i\frac{m}{x}}, \tag{5}$$

where:

$$c_m = \frac{1}{2\pi}\int_{x_0+h_1(x_0)}^{x_0} \frac{1}{x^2} f(x) e^{-i\frac{m}{x}} dx, x_0 \neq 0. \tag{6}$$

2.2. The discrete form of the Reciprocal Fourier Transform

Eq. (6) gives the coefficient of each term with different m in Eq. (5). For a given original signal $f(x)$ where $x \in [x_0, x_1]$ with a uniform sampling and a total sampling number of N, the sampled points are:

$$x_p = x_0 + \frac{p}{N}T, \tag{7}$$

where $T = x_1 - x_0$. Then, we have the discrete form of Eq. (6) since the original signal has a limited length:

$$c_m = \frac{1}{2\pi}\sum_{p=0}^{N} \frac{1}{x_p^2} f(x_p)\exp\left(-\frac{im}{x_p}\right). \tag{8}$$

Therefore, the coefficients c_m are available by taking the sum of the production of the sampled points and the corresponding basis. However, for a total scan number M of coefficient m, the algorithm requires $M \times N$ times multiplication processes.

Now, resample the signal by the following rule:

$$x_p = \frac{1}{\left(\frac{1}{x_0} - \frac{1}{x_1}\right)\frac{p}{N} + \frac{1}{x_1}}, \tag{9}$$

where N is the total number of the sampled points, p are integers from 0 to $N-1$. Substitute x_p in Eq. (9) for x in the basis $\exp(im/x)$, we have:

$$r_m = \exp\left\{im\left[\left(\frac{1}{x_0} - \frac{1}{x_1}\right)\frac{p}{N} + \frac{1}{x_1}\right]\right\} = \exp\left\{im\left[\left(\widetilde{x}_1 - \widetilde{x}_0\right)\frac{p}{N} + \widetilde{x}_0\right]\right\}, \tag{10}$$

where $\widetilde{x}_0 = 1/x_1$, and $\widetilde{x}_1 = 1/x_0$. Let

$$\widetilde{x}_p = \left(\widetilde{x}_1 - \widetilde{x}_0\right)\frac{p}{N} + \widetilde{x}_0, \tag{11}$$

we have $r_m = \exp(im\widetilde{x}_p)$. Therefore, by sampling the original signal according to Eq. (9) and mapping the function $f(x)$ to $g(\widetilde{x})$ following Eq. (10), we obtain the mapped signal which has the same form of a uniform sampling. Therefore, the algorithms developed for the

Fourier Transform can be directly used by the RFT. Due to the highly efficient FFT algorithm developed by Cooley and Tukey [30], the analyzing speed can be improved compared to using Discrete Reciprocal Fourier Transform (DRFT) given by Eq. (8) directly. In this paper, we call the algorithm following the sampling rule of Eq. (9) and analysis using the FFT method the Reciprocal Fast Fourier Transform (RFFT) method.

2.3. The application of the reciprocal Fourier transform in spectrum analysis

Here we focus on the application of the RFT in the spectrum analysis of optical interferometers. Take the Fabry-Pérot interferometer as an example. Fig. 1 shows the schematical drawing a typical Fabry-Pérot Interferometer. The incident light $\boldsymbol{E}_{\text{inc}}$ comes from the left side of Mirror 1. Part of the incident light ($\boldsymbol{E}_{\text{refl},1}$) is reflected by Mirror 1, and the rest portion ($\boldsymbol{E}_{\text{laun}}$) transmits into the cavity. In the cavity, the light will be reflected multiple times, and a stable state ($\boldsymbol{E}_{\text{circ}}$) will be generated due to the balance of the gain and the loss of the cavity. The light inside the cavity will leak through both Mirror 1 and Mirror 2 toward the opposite direction ($\boldsymbol{E}_{\text{back}}$) and the same direction ($\boldsymbol{E}_{\text{trans}}$) of the incident light.

Ismail *et al.* [26] analyzed the spectrum of F-P cavities. Consider the reflected light, according to the results given by Ref. [26], we have:

$$A = R_1 + \frac{T_1^2 R_2}{1 + R_1 R_2 - 2\sqrt{R_1 R_2}\cos(2\varphi)}. \tag{12}$$

where R_1 and R_2 are reflectivity of Mirror 1 and Mirror 2, respectively. $T_1 = 1 - R_1$ and $T_2 = 1 - R_2$ are transmissivity of Mirror 1 and Mirror 2, respectively. $\varphi = 2\pi nl/\lambda$ where l is the geometric distance between Mirror 1 and Mirror 2, n is the refractive index of the material filled in the cavity, and λ is the wavelength of light in vacuum. Hereinafter, we will call the multiplication of n and l the optical cavity length. To simplify the analysis process, rewrite Eq. (12) as

$$A(\lambda) = a + \frac{b}{c - d\cos(s/\lambda)}, \tag{13}$$

where $a = R_1$, $b = T_1^2 R_2$, $c = 1 + R_1 R_2$, $d = 2\sqrt{R_1 R_2}$, and $s = 4\pi nl$. Since

$$c - d\cos(s/\lambda) = \left(1 - \sqrt{R_1 R_2}\right)^2 + 2\sqrt{R_1 R_2}[1 - \cos(s/\lambda)] > 0, \tag{14}$$

the denominator of Eq. (13) is always positive.

Because the spectrum of an FPI is a function of the optical cavity distance nl, it is always used as displacement sensors or refractive index sensors. In this case, we need to calculate nl from the spectrum given by the spectrometer. Although the term $\cos(s/\lambda)$ is in the denominator of the signal $A(\lambda)$, the variable period of $A(\lambda)$ is the same as $\cos(s/\lambda)$. Therefore, RFT is a proper decomposition of $A(\lambda)$. Resample the spectrum $A(\lambda)$ according to Eq. (9) in wavelength range $[\lambda_0, \lambda_1]$ with a total sampling number of N. The mapped function $g\left(\widetilde{\lambda}\right)$ is uniformly sampled in section $\left[\widetilde{\lambda}_0, \widetilde{\lambda}_1\right]$ with the same sampling number N. The sampling frequency of $g(\widetilde{x})$ is:

$$f_s = \frac{N}{\widetilde{\lambda}_1 - \widetilde{\lambda}_0} = \frac{N\lambda_0\lambda_1}{\lambda_1 - \lambda_0}. \tag{15}$$

Therefore, the resolution is [31]:

$$R_r = \frac{f_s}{N} = \frac{\lambda_0\lambda_1}{\lambda_1 - \lambda_0}. \tag{16}$$

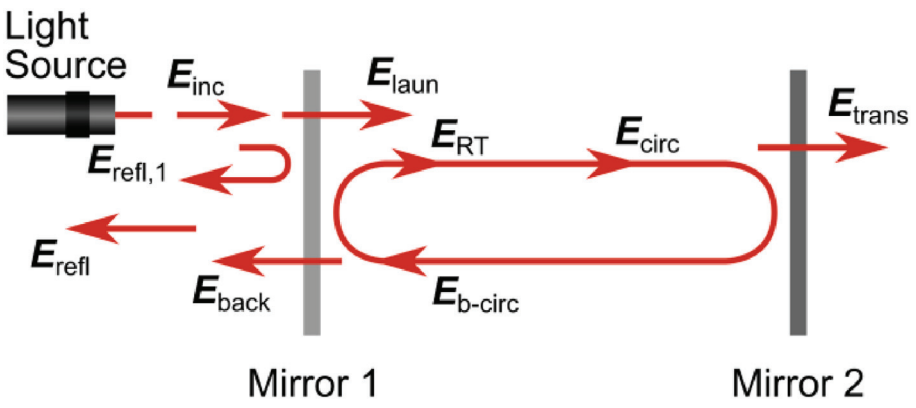

Fig. 1. Typical structure of an FPI.

Then, the resolution of the optical distance of the FPI is:

$$R_{\mathrm{rnl}} = \frac{R_{\mathrm{r}}}{2} = \frac{\lambda_0\lambda_1}{2(\lambda_1 - \lambda_0)}. \tag{17}$$

Due to the highly efficient FFT algorithm, the RFFT method can be an efficient way to calculate the optical distance between two mirrors of the FPI. However, the resolution highly depends on the wavelength range of the spectrometer according to Eq. (17) which may be a restriction of the applications that requires a high resolution.

2.4. Combination of the RFFT method and the cross-correlation method

The resolution of RFFT is limited to the wavelength range of the spectrometer, which cannot be easily improved for a given device. Therefore, it will be used as a rough estimation of the optical cavity length for further analysis. Assume that the spectrometer takes N uniformly spaced samples with respect to wavelength. The wavelength range of the spectrometer is $[\lambda_0, \lambda_1]$. Therefore, the wavelength resolution of the spectrometer is:

$$R_{\mathrm{s}} = \frac{\lambda_1 - \lambda_0}{N}. \tag{18}$$

Interpolate the spectrum obtained from the spectrometer using Eq. (9) to obtain a resampled dataset. The optical distance can then be determined by applying RFFT, and the resolution can be calculated using Eq. (17). Denote x_{R} as the optical distance given by RFFT. If we **assume the peak of the RFFT result has a symmetric shape between the maximum point**, the correct optical distance should be in range:

$$nl = [x_{\mathrm{R}} - R_{\mathrm{rnl}}/2, x_{\mathrm{R}} + R_{\mathrm{rnl}}/2]. \tag{19}$$

Focus on the minimum points (troughs) of the spectrum, we have $\cos(s/\lambda) = 1$ and therefore:

$$\lambda = \frac{2nl}{q}, q = 1, 2, 3\cdots \tag{20}$$

Since $\lambda \in [\lambda_0, \lambda_1]$, we have:

$$q \in \left[\frac{2nl}{\lambda_1}, \frac{2nl}{\lambda_0}\right]. \tag{21}$$

Substitute Eq. (19) into Eq. (21), we have:

$$q \in \left[\frac{2x_{\mathrm{R}} - R_{\mathrm{rnl}}}{\lambda_1}, \frac{2x_{\mathrm{R}} + R_{\mathrm{rnl}}}{\lambda_0}\right]. \tag{22}$$

According to Eq. (20), we have $nl = q\lambda/2$. Therefore, the resolution of the optical distance nl is:

$$R_{\mathrm{nl}} = \frac{qR_{\mathrm{s}}}{2}. \tag{23}$$

To improve the resolution, calculate the theoretical spectra with optical distances in the range given by Eq. (20) with a constant increment, and calculate the cross-correlation (xCor) between the theoretical spectra and the experimental spectrum. Then the number of the theoretical spectra M should be:

$$M = \frac{R_{\mathrm{rnl}}}{R_{\mathrm{nl}}} = \frac{N\lambda_0\lambda_1}{q(\lambda_1 - \lambda_0)} \in \left[\frac{2N/\lambda_1}{\left[4x_{\mathrm{R}}\left(\frac{1}{\lambda_0} - \frac{1}{\lambda_1}\right) + 1\right]\left(\frac{1}{\lambda_0} - \frac{1}{\lambda_1}\right)}, \frac{2N/\lambda_0}{\left[4x_{\mathrm{R}}\left(\frac{1}{\lambda_0} - \frac{1}{\lambda_1}\right) - 1\right]\left(\frac{1}{\lambda_0} - \frac{1}{\lambda_1}\right)}\right] \tag{24}$$

Take the maximum number, we have:

$$M_{\max} = \frac{2N/\lambda_0}{\left[4x_{\mathrm{R}}\left(\frac{1}{\lambda_0} - \frac{1}{\lambda_1}\right) - 1\right]\left(\frac{1}{\lambda_0} - \frac{1}{\lambda_1}\right)}. \tag{25}$$

Eq. (25) is the scan number to achieve the maximum resolution. If the requirement of the resolution is lower than the maximum resolution which is given in Eq. (23), the value of M can be reduced. In this case, the scan number is given by:

$$M = \frac{\lambda_0\lambda_1}{R_{\mathrm{rq}}(\lambda_1 - \lambda_0)}, \tag{26}$$

where R_{rq} is the requirement of the resolution. R_{rq} should not be larger than R_{nl} given in Eq. (23) as limited by the wavelength resolution of the spectrometer.

3. Results and discussion

In this section, we will evaluate and discuss the proposed methods in the context of specific problems. Firstly, we will compare and discuss the RFFT and FFT methods. The RFFT method effectively reveals the structure of the test function, whereas its FFT counterpart fails to disclose important structural information. Then, a noisy experimental spectrum will be analyzed using the proposed method, illustrating how to apply this method for real application. Finally, we will use the proposed method to provide real-time monitoring of an ECM process.

3.1. Comparison between the reciprocal Fourier transform and the Fourier transform

To compare the transform result of RFFT and FFT, we take transform of the test function:

$$f(x) = \cos\left(3 \times \frac{2\pi}{x}\right) + 1.5\sin\left(10 \times \frac{2\pi}{x}\right) \tag{27}$$

using both methods. We sample the function in $x \in [0.1, 0.5]$ with $N = 100000$. Fig. 2 shows the original signal, which exhibits a rapid oscillation near $x = 0.1$ and a slow oscillation close to $x = 0.5$. Our purpose is trying to reconstruct Eq. (27) from Fig. 2 using the proposed method and the FFT method.

Fig. 3 a) shows the transform using the RFFT method, with only frequencies in the range [0,20] displayed because the amplitudes of other frequencies are zero. The transformed signal agrees with the original function Eq. (27) since only frequencies at $m = 3$ and $m = 10$ have non-zero amplitudes of 1.0 and 1.5, respectively. Therefore, the original signal given by Eq. (27) can be reconstructed. In contrast, Fig. 3 b) shows the result obtained when FFT was applied directly to the signal in Fig. 2. Multiple peaks are visible, especially between 0 and 300, due to the use of an "improper basis" that cannot reflect the variable period of the original signal, which is now a function of x instead of a constant value. Therefore, the original signal can only be reconstructed when a proper basis is selected.

3.2. Application in spectrum analysis of a Fabry-Pérot interferometer

An experimental spectrum was analyzed to evaluate the performance of the proposed method. First, RFFT was used to provide an estimate of the optical distance of the FPI. Then, xCor was used to obtain a higher-resolution result. We used a Dell Precision 7520 workstation (Processor: Intel(R) Core(TM) i7-7820HQ CPU @ 2.90 GHz; installed RAM: 48.00 GB) to run the analysis. The spectrum, which includes 16,001 sampling points, was analyzed 1000 times with a resolution of the optical cavity length of 1 nm. The average processing time for each spectrum was 0.148 s, with a maximum of 0.337 s, a minimum of 0.114 s, and a standard deviation of 0.039 s. The optical cavity length of the spectrum was calculated to be 223.68 μm. Fig. 4 shows the analyzing result of the proposed method. Fig. 4 a) shows the RFFT result of the experimental spectrum. We observe a peak at a cavity length of 220.92 μm with a resolution of 11.05 μm, which suggests that the cavity length should be in the range of [215.40, 226.45] μm. Fig. 4 b) shows the xCor results within the range determined by the RFFT method. And Fig. 4 c) shows the theoretical and the experimental spectrum. As we can see, the theoretical and the experimental spectra match well and therefore the optical distance of the experimental spectrum should be close to that of the theoretical spectrum.

3.3. Application in electrochemical process monitoring

3.3.1. Materials and equipment

In the ECM monitoring experiment, $NaNO_3$ solution with a concentration of 13 % (w/w) was used as electrolyte. $NaNO_3$ was purchased from Millipore Sigma (molecular weight: 84.99, form: crystal). Two linear stages (OptoSigma, OSMS 20–35) were used to

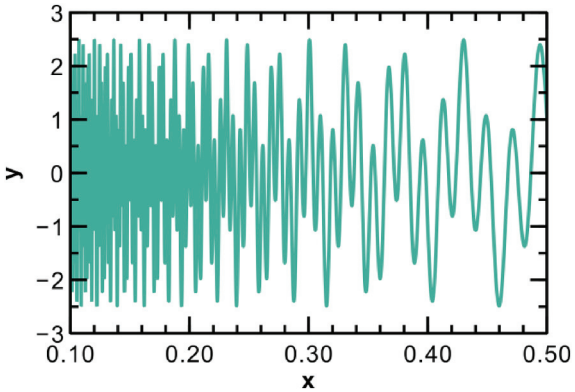

Fig. 2. The original signal to be transformed.

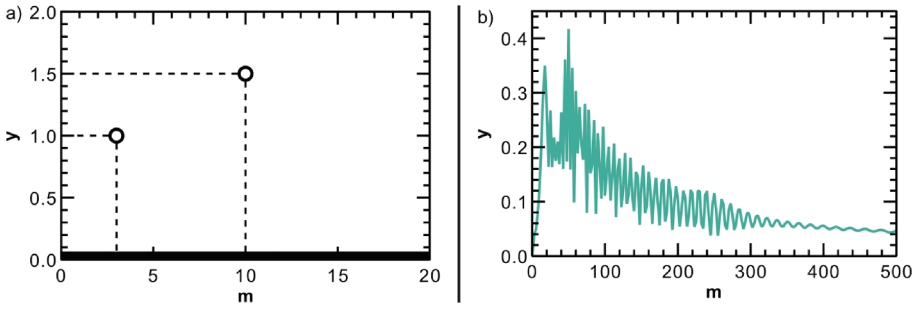

Fig. 3. Transform of the original signal using a) Reciprocal Fourier Transform and b) Fourier Transform.

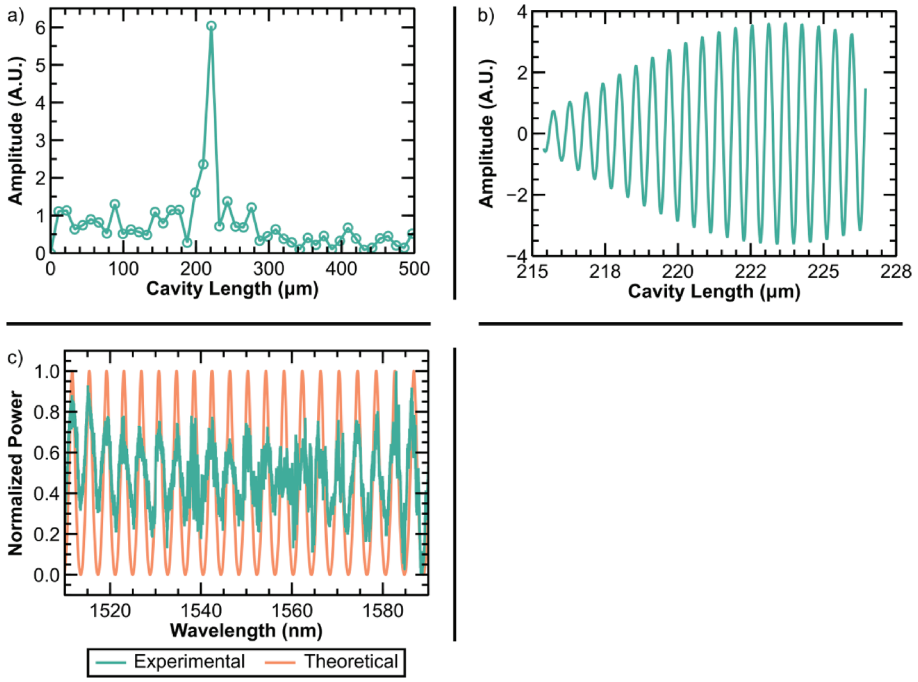

Fig. 4. Calculation of the cavity length of an experimental spectrum using the proposed method. a) The RFFT result of the experimental data with a peak at 220.92 μm; b) the cross-correlation between the experimental spectrum and the theoretical spectra with a cavity length range given by a); c) comparison between the experimental spectrum and the theoretical spectrum given by the proposed method.

control the movement of the tool. A DC power supply was used to provide constant electricity. A microcontroller (Arduino Uno R3) and a relay (SONGLE, model: SRD-05VDC-SL-C) were used to control the ON/OFF status of the power supply. An interrogator (MICRON OPTICS, model: sm125) was used to generate broadband light and give the spectrum of the FPI. A water pump (Kamoer, model: KLP01) was used to generate electrolyte flow. The reaction chamber was printed using a 3D printer (Sindoh 3DWOX DP201) with PLA (100 % infill rate). The optical system used to measure the machining depth consists of a nanometer scale positioning system (ALIO, hybrid hexapod) and an optical microscope (lens: Mitutoyo M Plan Apo 20x, camera: AmScope FMA050).

The refractive index of the electrolyte was measured before the machining process using an FPI with a known geometric cavity length l_1. This FPI was immersed in the electrolyte and the optical distance between the two reflection surfaces l_n was calculated. Therefore, the refractive index of the electrolyte was $n = l_n/l_1 = 1.3633$.

3.3.2. *Experimental results*

In this section, we introduce an application of the proposed method in electrochemical reaction monitoring. Electrochemical machining (ECM) is a process that removes material from a workpiece by electrochemical etching. During the process, the workpiece is connected to the anode of the power source, and the tool is connected to the cathode. A small gap, called the inter-electrode gap (IEG), should be maintained between the tool and the workpiece. To monitor this gap, which is about 200 μm in size in this research, optical fiber is one of the best candidates, as no metal is allowed in this gap. The electrolyte flows through the gap at high speed, carrying away the bubbles and the sediment generated during the reaction process. To achieve the best machining performance, the IEG must be kept

at the optimal value during the machining process. We monitored the IEG by feeding a single-mode fiber (SMF) through the hole at the center of the tool, with its axis perpendicular to the surface of the workpiece. The end face of the SMF and the surface of the workpiece form an FPI, enabling us to monitor the distance between the SMF and the workpiece. However, due to the disturbance caused by the pump and the electrolyte flow, as well as the presence of bubbles and sediment, the spectrum is usually noisy and changes rapidly. Traditional peak-tracking algorithms can easily fail to track the peaks or troughs in such conditions. In this study, we first compared the proposed method with existing monitoring data and then conducted real-time monitoring of the IEG.

We used data from our earlier research [25], where the spectra were analyzed manually, to evaluate the performance of the proposed method. The results are shown in Fig. 5 a), where the manual method (red) and the proposed method (blue) are plotted. As shown in Fig. 5 a), the two curves mostly overlap except for some deviations at around 150 s, 200 s, and 300 s. To have a better comparison, Fig. 5 b) shows the difference between the two curves (red circles), where most of the differences lie within the range of ±2.5 μm, with only a few points beyond this range. Fig. 5 c) shows the experimental and theoretical spectra at 293 s (point #8, green), which is a typical point with a difference larger than ±2.5 μm in Fig. 5 b). Despite the significant noise on the left side of the experimental spectrum, the difference between the manual and the proposed method at this point is still smaller than 15 μm.

Since the accuracy of the proposed algorithm was found to be satisfactory, it was utilized for real-time monitoring of the IEG to provide control information to the control system. Fig. 6 a) shows the schematical drawing of the upgraded ECM system. Compared with that used in Ref. [25], the position of the tool can be adjusted by a linear stage according to the monitoring results so that the IEG was maintained at 200 μm with a tolerance of ±10 μm. A water pump was used to create electrolyte flow through the space between the tool and the workpiece. The workpiece was placed vertically, and the tool was placed horizontally so that the bubbles and the sediments could be easily removed by the electrolyte flow. The electrolyte flowed through a filter to remove sediments generated during the ECM process. Subsequently, a syringe with air sealed in the barrel was used to reduce pump-induced vibrations. The electrolyte then flowed through the gap between the tool and the workpiece to flush the sediments and the bubbles generated during the reaction process before returning to the beaker, as shown in Inset A. The anode of the power supply was connected to the workpiece and the cathode was connected to the tool. The on and off status of the power was controlled by an Arduino Uno and a relay. Fig. 6 b) shows the structure of the tool. An optical fiber was fed through and fixed on a stainless-steel ferrule. The stainless-steel ferrule was fixed on a stainless-steel tube using conductive epoxy. Therefore, the optical fiber moved with the tool so that the IEG equaled the distance between the fiber tip and the workpiece. A second optical fiber was used to monitor the movement of the tool as shown in Inset B. Before machining, the IEG was adjusted to 200 μm for this experiment. When the power was turned on, the spectrum became noisy due to the generation of bubbles and sediments. Therefore, the power was turned off after a period so that a better spectrum could be

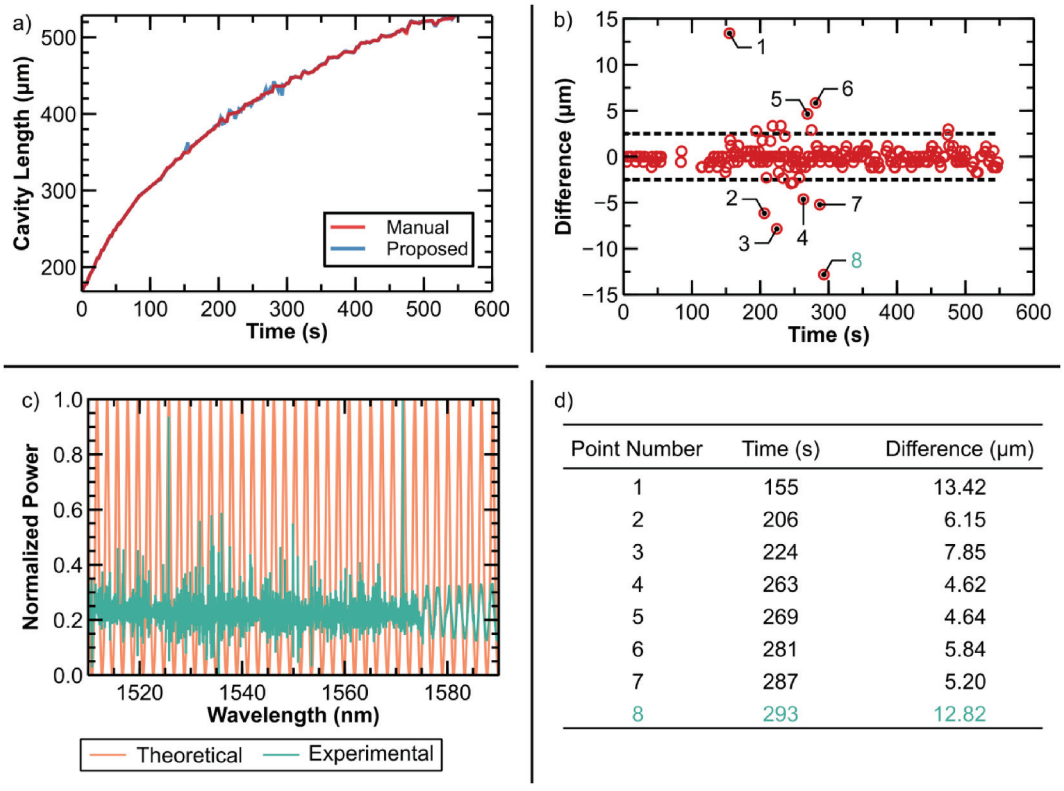

Point Number	Time (s)	Difference (μm)
1	155	13.42
2	206	6.15
3	224	7.85
4	263	4.62
5	269	4.64
6	281	5.84
7	287	5.20
8	293	12.82

Fig. 5. The cavity length of the F-P cavity used to monitor the ECM process analyzed manually and using the FSM method. a) the cavity lengths of manual and FSM methods; b) the difference between the manual method and the FSM method; c) theoretical and experimental spectra at 293 s (point # 8); d) information of the points that have a large difference.

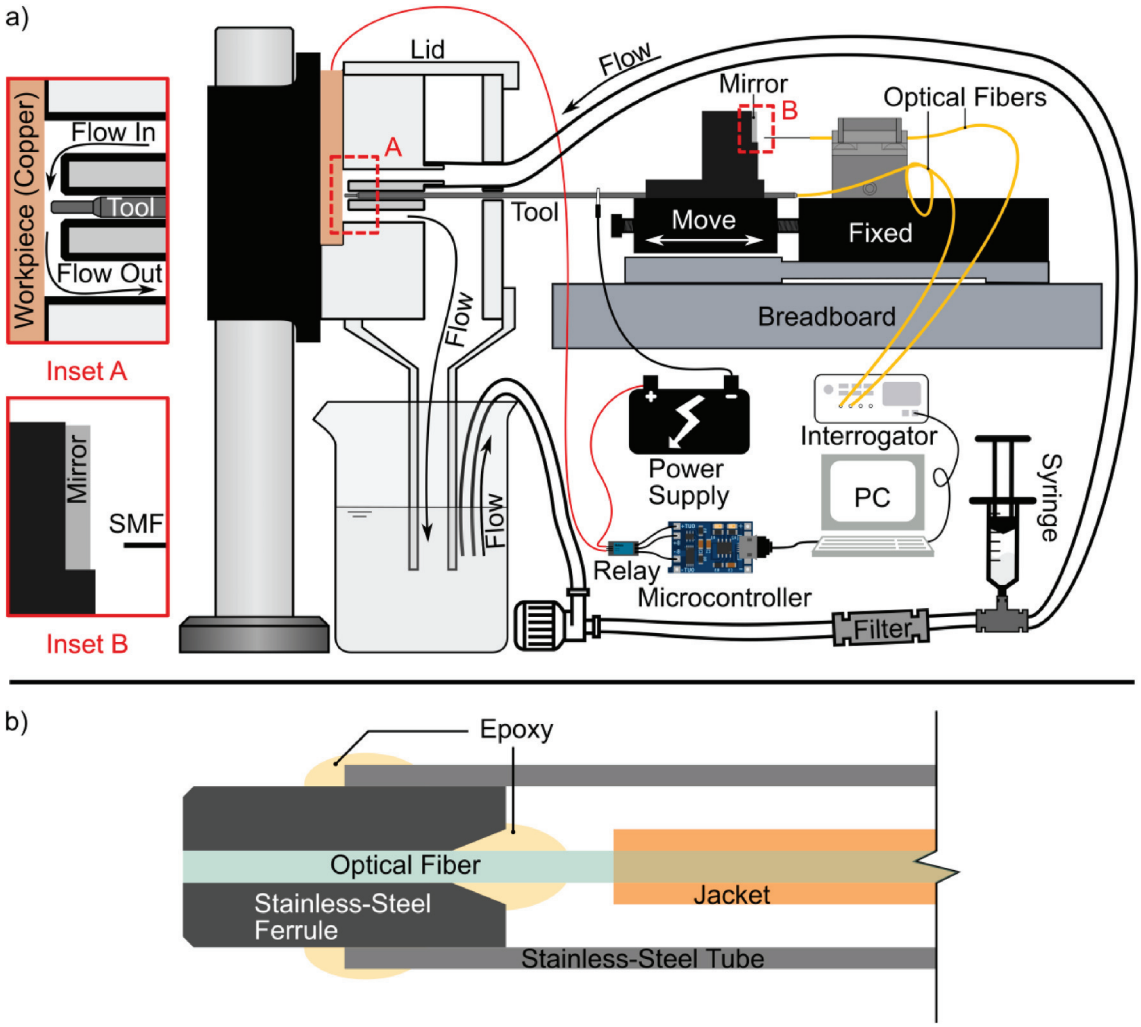

Fig. 6. ECM Machining system a) and design of the machining tool b).

collected and the IEG could be calculated. The spectra obtained during both the activation and deactivation of the power can be found in our earlier research Ref. [25]. After the measurement, the position of the tool was adjusted so that the IEG was maintained as a constant (200 μm). After the adjustment, we resumed the machining process by reactivating the power. This sequence was repeated

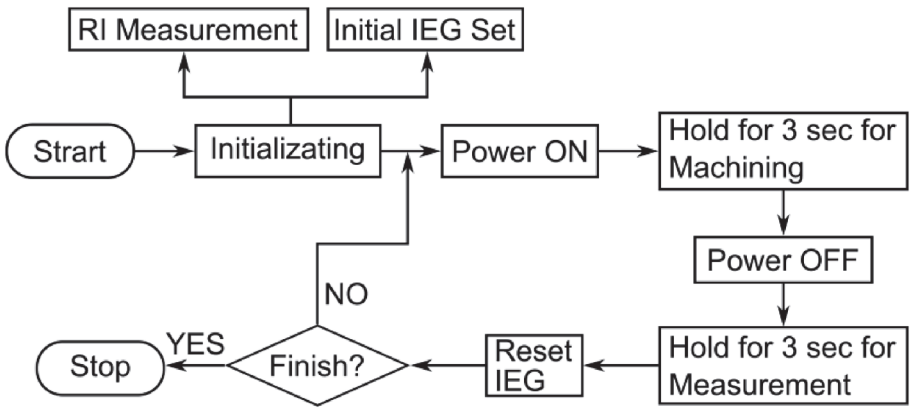

Fig. 7. Machining process for ECM monitoring.

until the machining depth reached the desired value.

Fig. 7 shows the flow chart of the ECM machining process. First, we need to initialize the system, including measuring the refractive index of the electrolyte and setting initial IEG as the setup IEG value which will be maintained throughout the machining process. Then, the power was turned on and the machining process was started. During the machining process, the spectrum was so noisy that no information could be extracted from it. Therefore, the power was then turned off for 3 s to reduce the noise so that the IEG could be measured. Due to the machining, the measured IEG will be larger than the setup IEG. Therefore, the IEG was adjusted so that the adjusted IEG equals the setup IEG. According to the measurement, the machining depth is also available. If the machining depth is smaller than the desired value, this process will be repeated. Otherwise, the machining process will be stopped.

The video in the supplementary material shows the monitoring and control process. The monitoring result of the ECM process is shown in Fig. 8. In this test, 5 V electric potential was applied on the tool and the workpiece. The $NaNO_3$ solution with a concentration of 13 % (w/w) was used as the electrolyte. As we can see, the machining depth (primary vertical axis, red) increased with time linearly with a slight decrease at around 65 min and recovered immediately as shown in the enlarged circle. This decrease was caused by the accumulation of sediment due to an insufficient electrolyte flow. Since the volume of the sediment is larger than that of the workpiece (Cu) which is etched by the reaction and the measurement given by the optical fiber sensor is now the distance between the fiber and the surface of the sediment, therefore the measured IEG reduced. After the sediment was flushed by the electrolyte, we can see the measured IEG increased immediately. This incident further proved the reliability of the proposed method. During the machining process, the IEG was set as a constant of 200 μm with a tolerance of ±5 μm. As we can see in Fig. 8 (secondary vertical axis, dark green), the IEG fluctuated within the expected range. At the end of the machining, the machining depth was measured as 2048 μm using the proposed method. Then, the machining depth was also measured with an optical system consisting of a nanometer scale positioning system (ALIO, hybrid hexapod) and an optical microscope (lens: Mitutoyo M Plan Apo 20x, camera: AmScope FMA050). The machining depth given by the optical system was 2044 μm. A difference of 4 μm was obtained which can mostly come from the change of refractive index of the electrolyte. Measurement error of both the optical system and the proposed method can be another source of error.

4. Conclusion

The proposed method presented in this research enables the calculation of the optical distance of the cavity of an FPI with high speed and high resolution. By expanding the spectrum with basis with variable period, the proposed method directly transforms the spectrum from wavelength to optical distance. In particular, the proposed method estimates the cavity length with the RFFT method, followed by taking cross-correlation between the theoretical spectra and the experimental spectrum within the estimated range to achieve high speed and high resolution. The effectiveness of the proposed method was demonstrated by monitoring the gap distance between the tool and workpiece electrodes during an electrochemical machining process using an FPI. By providing real-time distance feedback, the IEG was successfully maintained at a constant distance (200 μm) throughout the entire reaction process.

This method solves the following problems or have the following improvements compared with the traditional method that tracks the troughs/peaks of the spectrum (peak tracking method) or using FFT directly (FFT method):

1) The proposed method provides the absolute value of the optical distance.
2) The proposed method is robust to noise and abrupt changes in the spectrum.
3) The proposed method expands the spectrum with a basis have a similar mathematic structure (variable period) of the spectrum.
4) The proposed method provides acceptable measurement accuracy in real-time monitoring, even in harsh environments with chemical reactions, vibrations, bubbles, sediments, temperature fluctuations, and other factors.
5) The proposed method provides a reliable way to monitor the IEG of ECM process in real-time and with high precision.

The experiment underscores the potential application of an optical fiber Fabry-Pérot interferometer for monitoring the ECM process, which has been a challenge for scientists and engineers for more than 100 years. Furthermore, considering that the spectrometer employed in this experiment offers a theoretical resolution reaching the nanometer scale, this method also demonstrates significant promise for micro/nano ECM monitoring.

CRediT authorship contribution statement

Fengfeng Zhou: Writing – review & editing, Writing – original draft, Visualization, Validation, Supervision, Software, Methodology, Investigation, Formal analysis, Data curation, Conceptualization. **Siying Chen:** Validation, Methodology, Investigation, Data curation. **Xingyu Fu:** Writing – review & editing, Validation, Software, Data curation. **Martin B.G. Jun:** Writing – review & editing, Validation, Supervision, Resources, Methodology, Conceptualization.

Declaration of competing interest

The authors declare the following financial interests/personal relationships which may be considered as potential competing interests: Martin B. G. Jun reports financial support was provided by National Science Foundation.

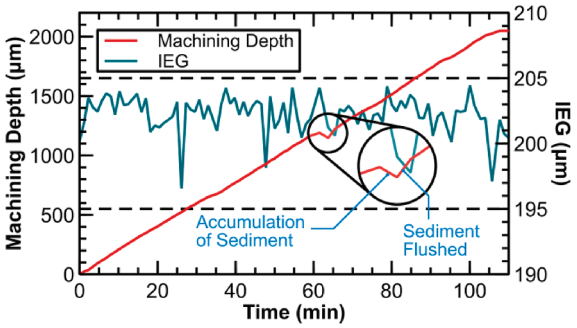

Fig. 8. Real-time monitoring of the ECM process. The red curve shows the machining depth with respect to time, and the green curve shows the IEG during the machining process. The inset shows the influence of the sediment accumulation to the measurement of the machining depth if not flushed sufficiently. (For interpretation of the references to colour in this figure legend, the reader is referred to the web version of this article.)

Data availability

Data will be made available on request.

Acknowledgements

This material is based upon work supported by the National Science Foundation under Grant No. NSF AM-2125826.
Funding: This work was supported by the National Science Foundation under Grant No. NSF AM-2125826.

References

[1] D.-J. Cheng, F. Xu, S.-H. Xu, C.-Y. Zhang, S.-W. Zhang, S.-J. Kim, Minimization of surface roughness and machining deformation in milling of Al alloy thin-walled parts, Int. J. Precis. Eng. Manuf. 21 (9) (2020) 1597–1613.
[2] J. Yi, et al., Prediction of mesoscale deformation in milling micro thin wall based on cantilever boundary, Int. J. Adv. Manuf. Technol. 106 (7) (2020) 2875–2892.
[3] L. Wang, H. Si, Machining deformation prediction of thin-walled workpieces in five-axis flank milling, Int. J. Adv. Manuf. Technol. 97 (9) (2018) 4179–4193.
[4] C.R. Chighizola, C.R. D'Elia, M.R. Hill, Intermethod comparison and evaluation of near surface residual stress in aluminum parts subject to various milling parameters, in: Residual Stress, Thermomechanics & Infrared Imaging and Inverse Problems, vol. 6, Springer, 2020, pp. 67–74.
[5] L. Meng, A.M. Khan, H. Zhang, C. Fang, N. He, Research on surface residual stresses generated by milling Ti6Al4V alloy under different pre-stresses, Int. J. Adv. Manuf. Technol. (2020) 1–12.
[6] J.A. García-Barbosa, E. Cordoba-Nieto, An approach to residual stress measurement in ball-end milling process on Ti-6Al-4V ELI titanium alloy, Int. J. Mach. Mach. Mater. 22 (3–4) (2020) 197–211.
[7] K.P. Rajurkar, B. Wei, C.L. Schnacker, Monitoring and control of electrochemical machining (ECM), J. Eng. Industry 115 (2) (May 1993) 216–223, https://doi.org/10.1115/1.2901652.
[8] D. Clifton, A.R. Mount, G.M. Alder, D. Jardine, Ultrasonic measurement of the inter-electrode gap in electrochemical machining, Int. J. Mach. Tool Manuf. 42 (11) (2002) 1259–1267, https://doi.org/10.1016/S0890-6955(02)00041-X.
[9] B.P. Abbott, et al., LIGO: the laser interferometer gravitational-wave observatory, Rep. Prog. Phys. 72 (7) (2009) 076901, https://doi.org/10.1088/0034-4885/72/7/076901.
[10] F. Acernese, et al., Advanced Virgo: a second-generation interferometric gravitational wave detector, Class. Quantum Grav. 32 (2) (2014) 024001, https://doi.org/10.1088/0264-9381/32/2/024001.
[11] T. Akutsu, et al., First cryogenic test operation of underground km-scale gravitational-wave observatory KAGRA, Class. Quantum Grav. 36 (16) (2019) 165008, https://doi.org/10.1088/1361-6382/ab28a9.
[12] Z. Gan, et al., Spatial modulation of nanopattern dimensions by combining interference lithography and grayscale-patterned secondary exposure, Light Sci. Appl. 11(1) (2022) Art. no. 1. doi: 10.1038/s41377-022-00774-z.
[13] G. Xue, et al., Polarized holographic lithography system for high-uniformity microscale patterning with periodic tunability, Microsyst. Nanoeng. 7(1) (2021) Art. no. 1. doi: 10.1038/s41378-021-00256-z.
[14] B. Zhang, et al., Self-organized phase-transition lithography for all-inorganic photonic textures, Light Sci. Appl. 10(1) (2021) Art. no. 1. doi: 10.1038/s41377-021-00534-5.
[15] A.T. Meek, et al., Real-time imaging of cellular forces using optical interference, Nat. Commun. 12(1) (2021) Art. no. 1. doi: 10.1038/s41467-021-23734-4.
[16] M. Berardi, et al., Optical interferometry based micropipette aspiration provides real-time sub-nanometer spatial resolution, Commun. Biol. 4(1) (2021) Art. no. 1. doi: 10.1038/s42003-021-02121-1.
[17] G. Wissmeyer, M. A. Pleitez, A. Rosenthal, V. Ntziachristos, Looking at sound: optoacoustics with all-optical ultrasound detection, Light Sci. Appl. 7(1) (2018) Art. no. 1. doi: 10.1038/s41377-018-0036-7.
[18] Y.-N. Pang, et al., Singlemode-multimode-singlemode optical fiber sensor for accurate blood pressure monitoring, J. Lightwave Technol. (2022) 1–1. doi: 10.1109/JLT.2022.3155194.
[19] C.M. Harvey, K. Mühlberger, M. Fokine, Mach-Zehnder interferometer for in-situ non-contact temperature monitoring during thermal processing of an optical fibre, J. Lightwave Technol. 39 (22) (2021) 7223–7230.
[20] S. Wu, L. Wang, X. Chen, B. Zhou, Flexible optical fiber Fabry-Perot interferometer based acoustic and mechanical vibration sensor, J. Lightwave Technol. 36 (11) (2018) 2216–2221, https://doi.org/10.1109/JLT.2018.2810090.
[21] F. Zhou, H. Su, H.-E. Joe, M.-B.-G. Jun, Temperature insensitive fiber optical refractive index probe with large dynamic range at 1,550 nm, Sens. Actuators A (2020) 112102.
[22] F. Zhou, J.-T. Tsai, S. Jo, G. Kim, P.C. Lee, M.B.-G. Jun, In-situ monitoring of solidification process of PVA solution by fiber optic sensor technique, IEEE Sens. J. (2020) 1–1. doi: 10.1109/JSEN.2020.3040571.
[23] H.E. Joe, F. Zhou, S.T. Yun, M.B.G. Jun, Detection and quantification of underground CO2 leakage into the soil using a fiber-optic sensor, Opt. Fiber Technol. 60 (2020) undefined-undefined. doi: 10.1016/j.yofte.2020.102375.

[24] N.H. Maniya, D.N. Srivastava, Fabrication of porous silicon based label-free optical biosensor for heat shock protein 70 detection, Mater. Sci. Semicond. Process. 115 (2020) 105126, https://doi.org/10.1016/j.mssp.2020.105126.
[25] F. Zhou, W. Duan, X. Li, J.-T. Tsai, M.B.G. Jun, High precision in-situ monitoring of electrochemical machining process using an optical fiber Fabry-Pérot interferometer sensor, J. Manuf. Process. 68 (2021) 180–188, https://doi.org/10.1016/j.jmapro.2021.07.010.
[26] N. Ismail, C.C. Kores, D. Geskus, M. Pollnau, Fabry-Pérot resonator: spectral line shapes, generic and related Airy distributions, linewidths, finesses, and performance at low or frequency-dependent reflectivity, Opt. Express 24 (15) (2016) 16366–16389.
[27] T. Mizuno, T. Kitoh, M. Oguma, Y. Inoue, T. Shibata, H. Takahashi, Mach–Zehnder interferometer with a uniform wavelength period, Opt. Lett. 29(5) (2004) 454–456. doi: 10.1364/OL.29.000454.
[28] T. Mizuno, T. Kitoh, M. Oguma, Y. Inoue, T. Shibata, H. Takahashi, Uniform wavelength spacing Mach-Zehnder interferometer using phase-generating couplers, J. Lightwave Technol. 24 (8) (2006) 3217–3226, https://doi.org/10.1109/JLT.2006.876342.
[29] M.V. Pryjmak, Periodic functions with variable period, arXiv, arXiv:1006.2792, Jun. 2010. doi: 10.48550/arXiv.1006.2792.
[30] J.W. Cooley, J.W. Tukey, An algorithm for the machine calculation of complex fourier series, Math. Comput. 19 (90) (1965) 297–301, https://doi.org/10.2307/2003354.
[31] J. Semmlow, Signal analysis in the frequency domain—implications and applications, Circuits, signals and systems for bioengineers, pp. 169–206, 2018.